Int J Adv Manuf Technol (2018) 94:2981–2991
DOI 10.1007/s00170-017-1104-5

ORIGINAL ARTICLE

Critical condition prediction of adiabatic shear fracture in high-speed cutting TA2 alloy

Liyao Gu[1]

Received: 12 May 2017 / Accepted: 12 September 2017 / Published online: 22 September 2017

Abstract Titanium alloy, a special difficult-to-cut material, is hard to reach the occurrence of adiabatic shear fracture (ASF) in high-speed cutting. In this work, TA2 alloy was firstly taken as the workpiece in the high-speed cutting experiment under negative rake angle. The chip morphology transformation from serrated chip to isolated segment chip was obtained. The damage mechanism of ASF was investigated through scanning electron microscopic (SEM) observation on the fracture surface of isolated segment. Furthermore, based on saturation limit theory, the ASF prediction model was built up considering the conditions of stress, velocity, deformation, and constitutive relation. The critical cutting speed of ASF was predicted and verified experimentally. The influences of the cutting conditions and the thermomechanical properties on the occurrence of ASF were discussed. The results indicated that with the cutting speed increasing, the chip transformation from serrated chip to isolated segment chip was contributed to the periodic cycle of ASF. Comparing with other titanium alloys, TA2 alloy was more sensitive to ASF under negative rake angle and large feed.

Keywords Metal cutting · Saturation limit · Adiabatic shear fracture · Isolated segment

✉ Liyao Gu
guliyao0922@163.com

[1] Key Laboratory of Advanced Technologies of Materials, Institute of Materials Science and Engineering & State key Laboratory of Traction Power, School of Mechanics and Engineering, Southwest Jiaotong University, Chengdu, China

1 Introduction

High-speed machining technology is widely applied in most developing manufacture fields for the significant advantages of high precision, good surface quality, high efficiency, and low cost. With the cutting speed increasing, adiabatic shear evolution, including adiabatic shear instability, adiabatic shear banding (ASB), and adiabatic shear fracture (ASF) in primary deformation zone, is unavoidable. As the final stage of adiabatic shear evolution, the occurrence of ASF transforms the serrated chip to isolated segment chip, makes the cutting process discontinuous, and even brings about inevitable impacts on the machinabilities, such as cutting system chattering, cutting force fluctuation, tool failure, etc. Therefore, it is imperious to further investigate the fracture mechanism of isolated segment chip and construct an appropriate prediction model of ASF for the correct application in the practical cutting process.

The early studies mainly focused on adiabatic shear instability and localization laws under dynamical loading [1]. As for the formation and fracture mechanisms of serrated chip, the state-of-the-art studies have not yet reached a consensus understanding. The main opinions concentrated on adiabatic shear slipping theory and periodic cyclic fracture theory. Recht [2] and Komanduri [3] held that the thermoplastic instability-induced adiabatic shear slipping was the reason of serrated chip formation. The influences of rate-related characteristics and thermophysical properties on adiabatic shearing in serrated chip formation were revealed. Subsequently, the theory of adiabatic shear slipping-induced serrated chip formation was supported by more scholars [4–6]. As for the fracture mechanism of serrated chip, Shaw [7] proposed periodic cycle fracture theory to explain the catastrophic fracture in primary deformation zone of serrated chip. Elbestawi [8] and Poulachon [9] supported the periodic cycle fracture theory and considered that the work hardening and heat treatment effects on machined surface could

easily lead to brittle fracture in cutting hardened steel. Additionally, some scholars examined the microstructure on damaged ASB surface [5, 10, 11]. They found the formations of ductile dimple region and slipping region due to the shear deformation of primary deformation zone. Wang [12] found that the fracture could easily come up in the transformed band of high-strength steel. Su [13] hold that the brittleness enhancement in the work material led to the segment fracture through high-speed milling experiments. Hitherto, some studies addressed the fracture behavior in serrated chip formation through damage or fracture mechanical theories. Sowerby [14] adopted damage factor to predict the crack appearance during serrated chip formation through assessing the deformation, temperature, and stress states. Marusich [15] developed Lagranian model of machining AISI 4340 steel by continuous and adaptive meshing techniques to estimate crack propagation in serrated chip. Xie [16] indicated that the fracture of ASB in serrated could be estimated via flow localization parameter. The Johnson–Cook damage model was used by Guo [17] and Hua [18] to simulate the crack propagating process in serrated chip through applying FEM software. Recently, the saturation limit theory of ASF was first proposed by Gu and Wang [11, 19, 20] (GW theory) for revealing the ASF mechanisms in high-speed cutting.

In summary, the modeling and analysis on the occurrence of ASF is still a complicated and challenging work. As a special difficult-to-cut material, titanium alloy is hard to reach the occurrence of ASF in some high-speed cutting experiments [6]. In this work, we took TA2 alloy as the workpiece. The chip morphology transformation from serrated chip to isolated segment chip and the damage mechanism of ASF under negative rake angle were observed microscopically. Furthermore, considering the conditions of stress, velocity, deformation and constitutive relation, the prediction model of critical conditions of ASF was built up based on the proposed saturation limit theory. The theoretical results were verified through the cutting experiments. The sensitivities of cutting speed, feed, rake angel, and thermomechanical properties on the occurrence condition of ASF were discussed.

2 Experimental

2.1 Material and method

In the cutting experiments, a kind of industrial pure titanium (TA2 alloy) with poor machinability and wide application in the aerospace industry was selected as the to-be-cut material. The thermal physical properties of TA2 alloy are listed in Table 1. The metallographic structure of the material is shown in Fig. 1. The material matrix hardness was 58 HRA after vacuum annealing treatment, and the microstructure was composed of austenite blocks. The machining tests were carried out on Mill-Turn CNC by PCBN inserts under dry cutting condition in order to satisfy the orthogonal cutting condition. The cutting speed increased up until the isolated segment chip formation; the feed was 0.2–0.6 mm/r, and the tool rake angle was − 10°. The work material was machined into a cylindrical workpiece and fixed with the spindle. The obtained chips in the tests were embedded vertically into curing denture acrylic. The chip cross sections in the curing denture acrylics were polished and etched. The chip morphologies were examined through LEICA MeF-4 metallographic microscope. The fracture surface of the isolated segment chip was examined through scanning electron microscope (SEM).

Table 1 Thermophysical parameters of TA2 alloy

ρ (kg/m^3)	c (J/kg K)	k (W/m K)	T_m (K)	θ_0 (K)
4510	480	19.3	1942	300

2.2 Experimental results

Figure 2a shows the chip formation region of TA2 alloy via choosing proper cutting speed and feed intervals under the negative rake angle of − 10°. The critical regions of adiabatic shear and ASF are divided by the dotted line and the solid line, respectively. The corresponding chip formation region of isolated segments is on the right side of the solid line. At the cutting speed of 30 m/min and feed of 0.2 mm/r, the ribbon chip was obtained. When the cutting speed increased above 30 m/min, serrated chip began to develop. When the cutting speed increased to 1600 m/min, the isolated segment chip was generated. When the feed increased from 0.2 to 0.6 mm/r, the critical cutting speed of ASF decreased obviously. At feed of 0.6 mm/r, no ribbon chip was found. The macroscopic morphologies of serrated chip and isolated segment chip are shown in Fig. 2c, d. Although the increase of cutting speed

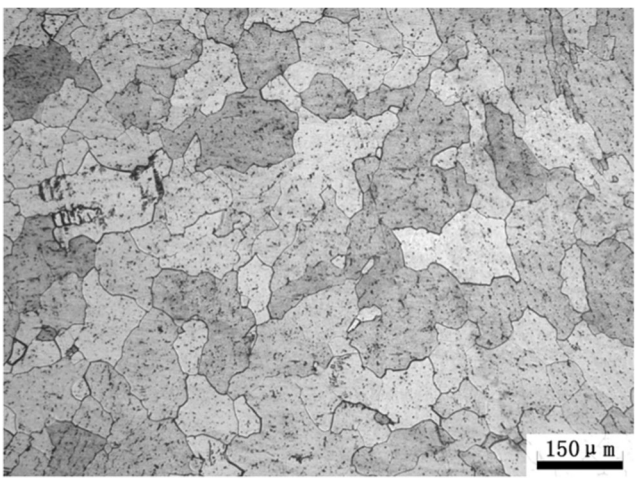

Fig. 1 Metallographic structure of TA2 alloy

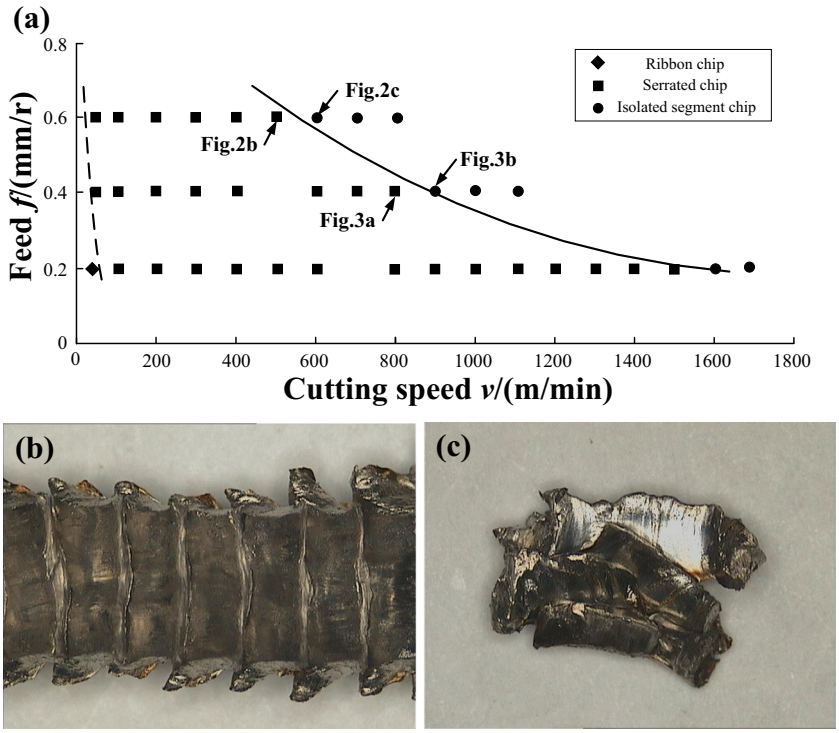

Fig. 2 The effect of cutting conditions on chip morphology in high-speed cutting TA2 alloy

leads to ASF and drives the serrated chip to the isolated segment chip, the negative rake angle can significantly enhance the sensitivity to the occurrence of ASF comparing with the work of Ye [21]. Moreover, the low negative rake angle increases the pressure stress. Thus, the negative rake angle decreases the critical cutting speed of ASF. Figure 3 shows the typical chip morphologies of serrated chip and isolated segment chip at the negative rake angle of − 10° and feed of 0.4 mm/r corresponding to Fig. 2a. The serrated chip segments fractured completely fracture along the transformed band and formed isolated segment chips. The result indicated that the transition from serrated chip to isolated segment chip was contributed to the periodic cycle of ASF. The temperature rise in the thin transformed band easily resulted in the reinforcement of ASB fracture toughness.

The damage mechanisms of ASF were inspected by SEM observations on the fractured surface of a single isolated segment. The SEM view direction is shown as Fig. 3b. The elongated ductile dimple region and smooth region that is covered with elongated dimples were examined along the shear direction as illustrated in Fig. 4a. The enlarged sites marked in Fig. 4a are shown in Fig. 4b–d. The ductile dimple structure was observed microscopically on the shear surface of serrated chip [22] and cup cone sample [23]. Due to the friction and pressure force near the tool tip under the high temperature, the dimples gradually faded away and lost the structure direction that resulted in the formation of smooth surface. The clue of melting state in ASB has not been found in SEM observation, but it may be detected in higher cutting speed. Accordingly, the ASF damage evolution during isolated segment formation of TA2 alloy can be described here. In stage I, the microvoids nucleated from inclusions, secondary phases or defects in band. The growing voids were

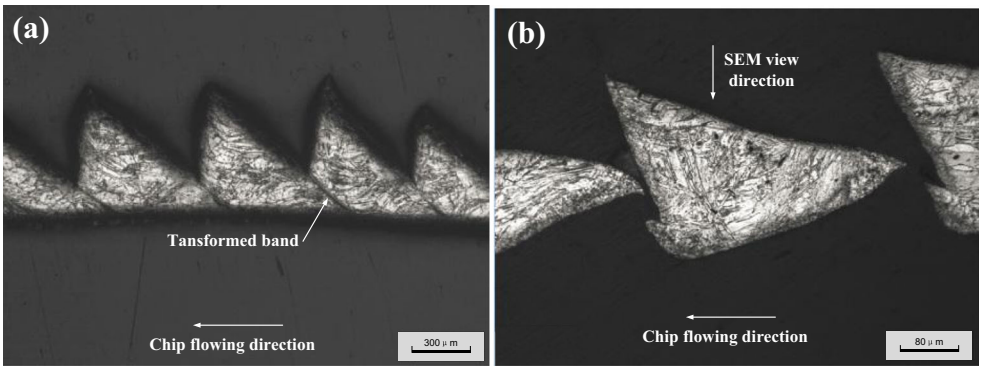

Fig. 3 The typical chip morphologies of **a** serrated chip and **b** isolated segment chip in high-speed cutting TA2 alloy

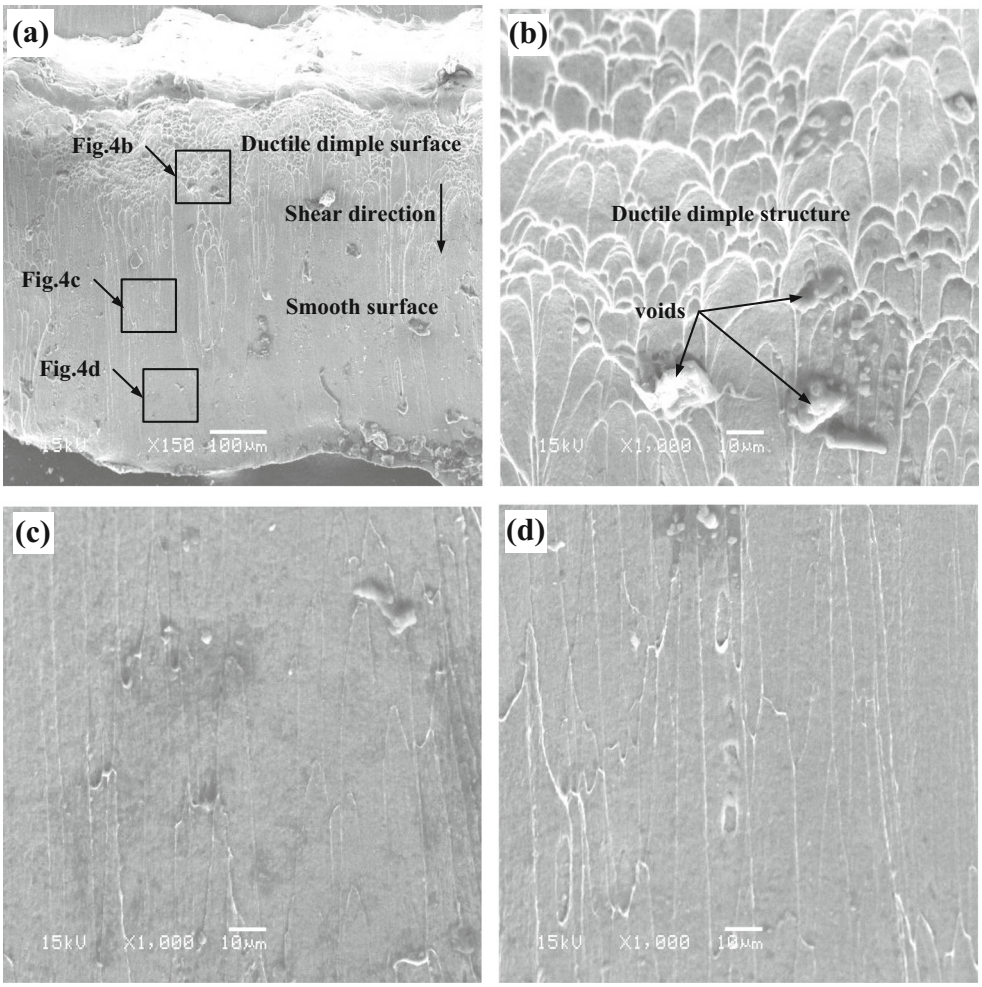

Fig. 4 SEM views of the fracture surfaces of isolated segment chip of TA2 alloy

elongated and rotated with the band deformation. The pressure stress near the tool tip would suppress the void development. In stage II, the ductile crack initiated and propagated via the void coalescence. Due to the coalescence of horizontally elongated flat voids, the new flat fracture surfaces with parabolic dimples were generated. In stage III, the ductile crack completely propagated along ASB under the severe heat concentration and friction between the two fractured surfaces. Therefore, the inhomogeneous distribution of stress and heat in PDZ led to various elongations of ductile dimple structure.

3 Theory

The orthogonal cutting condition under the plane strain state can effectively describe the chip formation and the dynamic mechanics behavior in primary deformation zone (PDZ). Based on this condition, the saturation limit criterion for the occurrence of ASF was proposed by Gu [11, 19] through considering the energy convergence in ASB. In the present work, we will predict the critical condition of ASF under negative rake angle.

3.1 Shear wave propagation

In order to analysis the wave propagation process in adiabatic shear evolution, flat wave fronts in this situation are considered here. The effects of wave reflection, refraction, and superposition should be ignored ideally under the continuous disturbance. Firstly, elastic shear wave (ESW) propagates at a constant speed of C_E from the loading side to the undeformed region when the disturbance imposed on the material in the elasticity range. Secondly, when the intensity of the disturbance imposed on the material exceeds its yield limit, plastic shear wave (PSW) generates rapidly at the loading side and propagates at the speed of C_P running after the ESW. Thirdly, when the localized effect of thermal softening in the rigid plastic region (RP region) exceeds the effects of strain and strain rate hardening, thermoplastic shear wave (TPSW) is generated in the weakest locus and propagated at the

speed of C_{TP}. As the loading and deformation of RP region cease, the propagation of TPSW decays gradually and forms ASB with a fixed width.

Due to the thermal softening effect and the cutting tool perturbation to the work material, the propagation model of PSW and TPSW under negative rake angle was built up as Fig. 5. v is the cutting speed; v_S is the shearing speed; $v_{ch}$is the chip flowing speed; $a_c$is the uncutting thickness; a_{ch} is the chip thickness; a_h is the sawtooth thickness; ϕ is the shear angle; l_S is the undeformed thickness of RP region; γ_0 is the tool rake angle; ξ is the wave front location of TPSW; h_S is the boundary location of PDZ. The red curve represents the stress–displacement relation, and the blue curve represents the displacement–time relation. The color depth varies with the gradient distribution of dynamic variables. U_y is the yield limit displacement. U_0 and t_0 are the displacement and the time of adiabatic shear instability, respectively. t_c is the time of ASF. In the model, the stress and velocity distributions of TP and RP regions in adiabatic shear evolution were considered. We assumed that the deformation process was adiabatic and the heat mainly concentrated in TP region; thus, only a small part of heat was conducted to RP region.

3.2 Stress state

The triaxiality stress state of TP region was considered during high-speed cutting process. The stress state of an infinitesimal element in TP region under the plane strain conditions was described via the principal stresses $[\overline{\sigma}_i]$, strain $[\overline{\varepsilon}_i]$, and strain rate $\left[\dot{\overline{\varepsilon}}_i\right]$ as

$$\begin{cases} \left[\overline{\sigma}_i\right] = \left[\dfrac{\sigma_{22}}{2} + (2-i)\sqrt{\dfrac{{\sigma_{11}}^2}{4} + \sigma_{12}^2}\right] \\ \left[\overline{\varepsilon}_i\right] = \left[(2-i)\sqrt{\varepsilon_{11}^2 + \dfrac{\varepsilon_{12}^2}{4}}\right] \\ \left[\dot{\overline{\varepsilon}}_i\right] = \left[(2-i)\sqrt{\dot{\varepsilon}_{11}^2 + \dfrac{\dot{\varepsilon}_{12}^2}{4}}\right] \end{cases} \tag{1}$$

According to Von–Mises yielding condition, the effective stress $\hat{\sigma}$, strain $\hat{\varepsilon}$, and strain rate $\hat{\dot{\varepsilon}}$ can be expressed as

$$\begin{cases} \hat{\sigma} = \dfrac{1}{\sqrt{2}}\sqrt{\sum_{i,j=1}^{3}\delta_{ij}\left(\overline{\sigma}_i - \overline{\sigma}_j\right)^2} \\ \hat{\varepsilon} = \dfrac{\sqrt{2}}{3}\sqrt{\sum_{i,j=1}^{3}\delta_{ij}\left(\overline{\varepsilon}_i - \overline{\varepsilon}_j\right)^2} \\ \hat{\dot{\varepsilon}} = \dfrac{\sqrt{2}}{3}\sqrt{\sum_{i,j=1}^{3}\delta_{ij}\left(\dot{\overline{\varepsilon}}_i - \dot{\overline{\varepsilon}}_j\right)^2} \end{cases} \tag{2}$$

where the subscript $i = 1, 2, 3$, and δ_{ij} is the Kronecker delta function. The effective shear stress $\hat{\tau}$, shear strain $\hat{\gamma}$, and shear strain rate $\hat{\dot{\gamma}}$ can be deduced as

$$\begin{cases} \hat{\tau} = \hat{\sigma}/\sqrt{3} \\ \hat{\gamma} = \sqrt{3}\hat{\varepsilon} \\ \hat{\dot{\gamma}} = \sqrt{3}\hat{\dot{\varepsilon}} \end{cases} \tag{3}$$

According to stress–displacement relation in the propagation model of stress waves, the flow stresses in TP region and RP region during the time $t_0 < t \le t_c$ can be given as

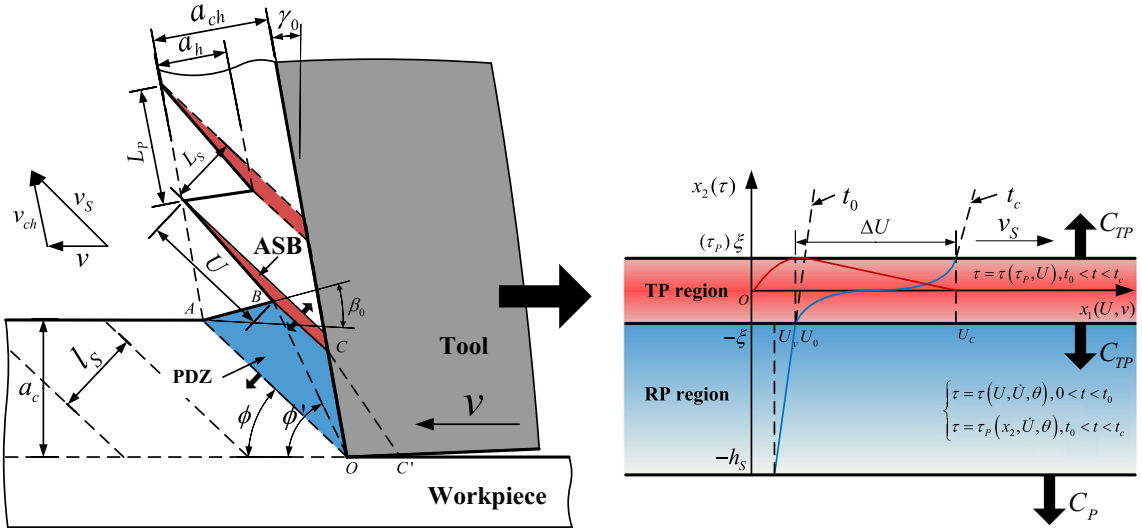

Fig. 5 Propagation model of the stress waves under negative rake angle in high-speed cutting

$$\begin{cases} \tau(x_2) \approx \tau(\tau_p, U), -\xi < x_2 \leq \xi \\ \tau(x_2) = \tau_P(x_2, \dot{U}, \theta), -h_S < x_2 \leq -\xi \end{cases} \tag{4}$$

where τ_p is the peak stress when adiabatic shear occurs; $\sigma = \tau \cot \phi$ is the relation between the pressure stress σ and the shear stress τ in PDZ. From the stress distributions of TP and RP regions, it could be seen that the stress of RP region reached the peak while the stress distribution in TP region was dependent on boundary displacement and peak stress.

3.3 Velocity distribution

According to the hodograph as shown in Fig. 5, the relations among the cutting speed of v (the speed of the tool relative to the workpiece), the chip flow speed v_{ch} (the speed of the chip relative to the tool), and the shear speed v_S (the speed of the chip relative to the workpiece) can be given as

$$\frac{v_{ch}}{v} = \frac{\sin\phi}{\cos(\phi - \gamma_0)}, \quad \frac{v_S}{v} = \frac{\cos\phi}{\cos(\phi - \gamma_0)} \tag{5}$$

The deformation process of ASB formation and fracture is different in adiabatic shear evolution [24]. The movement of the material in TP region and RP region was related with the wave front of TPSW and the boundary velocity of RP region. As the serrated chip developed, considering the gradient plastic law of adiabatic shear, the velocity distributions of TP region and RP region were given as

$$v_S(x_2) = \begin{cases} \dot{\gamma}_0 \left[x_2 - \frac{\xi}{\pi} \cos\left(\frac{x_2}{\xi} + \frac{1}{2} \right) \pi + \xi \right], & -\xi \leq x_2 < \xi \\ -\frac{v_S}{h_S - \xi}(x_2 + \xi), & -h_S \leq x_2 < -\xi \end{cases} \tag{6}$$

where $\dot{\gamma}_0 = v_S / 2\xi$ is the mean strain rate of TP region.

3.4 Deformation distribution

According to the physical model of isolated segment chip formation [11], the corresponding deformation model of isolated segment is shown in Fig. 5. Aiming at the deformation process of the segment *OABC*, when the cutting tool moves from the point C' to the point O, the work material point C' moves to the point C and the point B rotated on the point A. The angle β_0 is the incline angle to the free surface. The increase of incline angle β_0 leads to an increasing deformation in RP region. The shear angle increases periodically from ϕ to ϕ' in the formation of isolated segment. The differences of deformation rates in TP and RP regions induced the increase of boundary displacement U. After the microscopic examination on serrated chips, the teeth space of isolated segment was approximated to the boundary displacement. Thus, we obtained the relation

$$2a_\beta \beta_0 + \phi + \gamma_0 = \frac{\pi}{2} \tag{7}$$

where the coefficient $a_\beta \approx 1$ is the experimental constant for the balance of Eq. (7). The free surface incline angle β_0 can be obtained, and the angle ψ between the free surface plane and the shear plane was

$$\psi = \beta_0 + \phi \tag{8}$$

Since the incline angle β_0 is mainly influenced by shear angle ϕ under a constant rake angle, the decrease in shear angle ϕ increases the free surface incline angle β_0. Gente [6] found that the free surface incline angle β_0 was about 18.7° which could be verified in the speed range. The shear angle ϕ was approximated as

$$\phi = \arctan\left(\frac{\cos\gamma_0}{\xi - \sin\gamma_0} \right) \tag{9}$$

where $\xi = a_{ch}/a_c$ is the chip deformation coefficient and $\xi \approx 0.9 \sim 1$ in adiabatic shear evolution. According to the previous work of Ye et al. [21], the shear band space L_S between the segments during serrated segment formation was approximated as

$$L_S = \frac{2X^{3/4}}{(2-X)^{1/2}} \left(\frac{9\rho c^2 k}{\tau_y \alpha^2 \gamma_0^3} \right)^{1/4} \tag{10}$$

where $X \approx 1$ presents a fully mature ASB. α is the damage weakening coefficient due to thermal softening effect. The predicted results of the shear band space L_S have been verified in the published works [25, 26]. In actual deformation process of a single segment, the boundary displacement of ASB that was related to the teeth space can be calculated as

$$\begin{cases} U \approx L_P[\cot\psi \cos(\phi - \gamma_0) + \sin(\phi - \gamma_0)] \\ L_P = L_S \sin(\phi - \gamma_0) \end{cases} \tag{11}$$

The coefficient a_β can be determined through Eqs. (7) and (11). Thus, the mean strain and strain rate in ASB and RP region in time $t_0 \leq t \leq t_c$ were given as

$$\begin{cases} \gamma(x_2) = \frac{U}{S}, \dot{\gamma}(x_2) = \frac{v_S}{S} = \frac{v\cos\gamma_0}{S\cos(\phi - \gamma_0)}, -\xi \leq x_2 < \xi \\ \gamma(x_2) = \frac{\sin\beta_0}{\sin\phi\sin\psi}, \dot{\gamma}(x_2) = \frac{v_S}{L_S} = \frac{v\cos\gamma_0}{L_S\cos(\phi - \gamma_0)}, -h_S \leq x_2 < -\xi \end{cases} \tag{12}$$

From the expressions of velocity and deformation distribution of TP and RP regions, it was indicated that the velocity and deformation distributions were proximately linear in RP region, but were nonlinear in TP region.

3.5 Constitutive relation

The critical condition of the occurrence of ASF is influenced by the dynamic mechanic performance of work material which can be obtained via Split Hopkinson Pressure Bar (SHPB) test. The SHPB test was considered as a general and effective method that has been applied in the high-speed cutting process [17, 27]. According to the stress wave propagation theory based on the assumption of the strain impulse homogeneity, the strain, strain rate, and stress were expressed as

$$\begin{cases} \varepsilon(t) = \dfrac{2C_0}{L}\int_0^t \varepsilon_{\mathrm{R}}(t)\mathrm{d}t \\ \dot{\varepsilon}(t) = \dfrac{2C_0}{L}\varepsilon_{\mathrm{R}}(t) \\ \sigma(t) = E\left(\dfrac{A}{A_{\mathrm{S}}}\right)\varepsilon_{\mathrm{T}}(t) \end{cases} \tag{13}$$

where C_0 is the elastic wave speed, $\varepsilon_{\mathrm{R}}(t)$ is the strain impulse of reflected wave, $\varepsilon_{\mathrm{T}}(t)$ is the strain impulse of transmitted waves, A and A_{S} are the areas of the bar and sample, respectively, and L is the length of the work sample. The general thermoviscoplastic constitutive model is given as

$$\sigma\left(\varepsilon, \dot{\varepsilon}, \theta^*\right) = f_1(\varepsilon) f_2\left(\dot{\varepsilon}\right) f_3\left(\theta^*\right) \tag{14}$$

where $f_1(\varepsilon)$ is the component of strain hardening effect, $f_2\left(\dot{\varepsilon}\right)$ is the component of strain rate hardening effect, and $f_3(\theta^*)$ is the component of thermal softening effect.

The modified Johnson–Cook constitutive model of TA2 alloy was obtained through the SHPB tests under various impacting speeds and temperatures:

$$\sigma_{TA2} = \left[150 + 797\varepsilon^{0.75}\right]\left(1 + 0.1\ln\frac{\dot{\varepsilon}}{\dot{\varepsilon}_0}\right) \left[6.375\exp\left(-0.00461\theta^*\right)\right] \tag{15}$$

where $\dot{\varepsilon}_0$ is the reference strain rate and θ^* is the characteristic temperature.

3.6 Saturation limit theory

Based on the investigations of the chip morphology experiments and the influences of cutting conditions on ASF, the theoretical model for predicting the critical occurrence condition of ASF was built up in this section. Considering the momentum and energy conservation principles in TP region, the continuum governing equations in Lagranian coordinate system as illustrated in Fig. 6 were given as

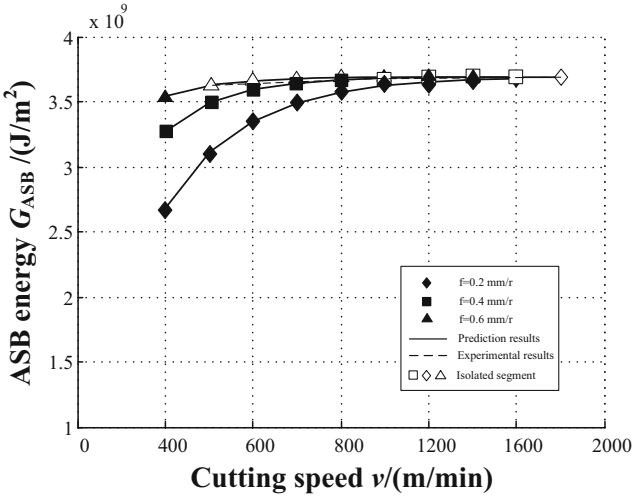

Fig. 6 The theoretical prediction and experimental results of ASB energy in high-speed cutting TA2 alloy

$$\begin{cases} \rho\dfrac{\partial v_S}{\partial t} = \dfrac{\partial \hat{\tau}}{\partial x_2} \\ \dfrac{\partial \theta}{\partial t} = \dfrac{\beta}{\rho c}\hat{\tau}\dot{\gamma} + \chi\dfrac{\partial^2\theta}{\partial x_2^2} \end{cases} \tag{16}$$

The propagation characteristic of TPSW can be determined through the competition of momentum and energy. The adiabatic temperature rise due to fast heating during adiabatic shear banding under high cutting speed can be expressed as

$$\theta = \frac{\beta}{\rho c}\int_0^{\gamma}\hat{\tau}\left(\gamma, \dot{\gamma}, \theta\right)\mathrm{d}\gamma + \theta_0 \tag{17}$$

The propagation functions of TPSW and the material evolution in TP region can be described via the continuum governing equations. The width of TP region and its energy dissipation can be determined. The kinematic equation of the wave front of TPSW was derived through momentum theorem

$$\frac{\mathrm{d}P(\xi)}{\mathrm{d}t} = 4\rho\dot{\gamma}\xi\dot{\xi} = \tau_{\mathrm{x}} - \hat{\tau}\left(U, \dot{U}, \theta^*\right), \begin{cases} x = \mathrm{y} \ \left(t_y < t \le t_0\right) \\ x = p \ \left(t_0 < t \le t_c\right) \end{cases} \tag{18}$$

where the subscript x presents the formation and fracture of TP region.

According to the high rate loading experiments [28, 29] and the analysis of linearized deformation of TP region, the post-peak performance of TP region can be linearized as

$$\hat{\tau}\left(U, \dot{U}, \theta\right) \approx \tau_x\left(1 - \frac{\tau_x}{\Delta W}\Delta U\right) \tag{19}$$

where U is the boundary displacement of TP region and W is the boundary shear work of TP region. The deformation focused on TP region when serrated chip forms; thus, the compatible movement condition of TP region was given as

$$\Delta U = U - U_x = \int_{t_x}^{t} 2\dot{\gamma}_0 \xi \mathrm{d}t \tag{20}$$

Considering the kinematic law and boundary condition $\Delta \dot{U}_0 = \Delta U_0 = 0$, the TPSW front location ξ and the stress collapsing time Δt_c during isolated segment chip formation were solved

$$\xi_c = \frac{3\tau_p^2 \Delta t^2}{4\rho \Delta W_c}, \Delta t_c = \frac{1}{\tau_p}\left(\frac{18\rho \Delta W_c^2}{\dot{\gamma}_c}\right)^{1/3} \tag{21}$$

Considering the damage weakening effect due to thermal softening effect in TP region, the post-peak constitutive relation was given by

$$\hat{\tau} = \tau_P[1-\alpha(\theta)] \tag{22}$$

The rate of temperature rise can be approximated as

$$\frac{\partial \theta}{\partial t} \approx \frac{1}{\partial \tau_S / \partial \theta^*}\frac{\tau_S - \tau_p}{\Delta t} = \frac{\theta(t)}{\Delta t} \tag{23}$$

The critical temperature rise of TP region through the energy equation was approximated as

$$\Delta \theta_c \approx \frac{\tau_p \dot{\gamma}}{\rho c}\Delta t_c - \chi \frac{\partial^2 \theta}{\partial y^2}\Delta t_c \tag{24}$$

where the strain energy component and the heat conduction component can be estimated as $\tau_p \dot{\gamma} \Delta t_c \approx \tau_p \Delta U_c / 2\xi = \Delta W_c / 2\xi$ and $\partial^2\theta/\partial y^2 \approx \Delta\theta_c / 4a\xi^2$ [26]. According to the minimum energy dissipation principle, the minimum energy from the shear band formation to fracture with the condition $d\Delta W_c / d\xi = 0$ can be deduced as

$$\Delta W_m = 4\rho c \Delta \theta_c \xi_c \tag{25}$$

Thus, the corresponding shear bandwidth S_c and the critical collapsing time Δt_c were

$$\begin{cases} S_c = 2\xi_c = 2\left(\dfrac{9\rho^3\chi^3 c^2 \Delta\theta_c^2}{2a^3\tau_P^3\dot{\gamma}_c}\right)^{1/4} \\ \Delta t_c = \dfrac{6\rho c \Delta\theta_c}{\tau_P}\left(\dfrac{\rho\chi}{2a\tau_P\dot{\gamma}_c}\right)^{1/2} \end{cases} \tag{26}$$

where factor a can be obtained according to shear bandwidth [30].

The saturation limit G_{ASB}^f can be calculated by the sum of pre-peek energy G_0 and post-peak energy G_P

$$G_{ASB}^f = G_0 + G_P = \int_0^{\gamma_0} \hat{\tau} d\gamma + 6\rho c \Delta\theta_c \left(\frac{\rho\chi\dot{\gamma}_c}{2a\tau_p}\right)^{1/2} \tag{27}$$

The occurrence criterion of ASF during high-speed cutting was given as

$$G_{ASB} \geq G_{ASB}^f \tag{28}$$

where $G_{ASB} = \int_0^{\gamma_c} \hat{\tau}(\gamma, \dot{\gamma}, \theta) d\gamma$ is the energy concentration in ASB. As the shear band development, the energy in ASB increases. When the energy in ASB reaches the saturation limit, the ASB is regarded as being fractured. We defined saturation degree D_{ASB} to describe the degree of shear band development,

$$D_{ASB} = \frac{G_{ASB}}{G_{ASB}^f} \tag{29}$$

When the saturation degree D_{ASB} reaches one, the ASB energy attains to saturation limit.

4 Results and discussions

According to the theoretical prediction model of ASF presented in Section 3, the energy convergence in ASB was mainly dependent on the cutting speed, the rake angle, and the cutting thickness. Thus, the critical occurrence of ASF can be determined by the cutting variables based on saturation limit theory. The theoretical prediction process on the critical cutting speed of ASF was constructed through the calculations of strain, strain rate, and temperature and energy in ASB. With the cutting speed increasing, the energy concentration in ASB increased and reached limit energy as shown in Fig. 6. Based on the experimental results, the predicted critical cutting conditions of ASF under the negative rake angle are shown in Fig. 7. The upside and the downside of the critical curves

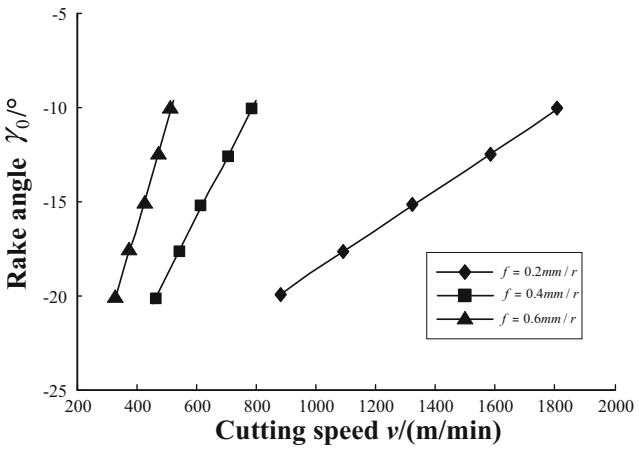

Fig. 7 The theoretical prediction results of ASF in high-speed cutting TA2 alloy

represent the unfractured serrated chip and isolated segment chip.

According to saturation limit theory, lower thermal conductivity leads to larger quantities of heat convergence in band and enhances the plasticity in the work material. The shear band material was not easy to reach the saturation limit due to thermal softening effect under high-temperature condition. Thus, the occurrence of ASF was difficult in a short segment forming time. In the cutting tests, the heat in chip with small thickness was observably influenced by the cutting tool; thus, the ASB energy converges were easier comparing with the theoretical results. Theoretically, the chip with small cutting thickness needs ASB to converge more energy through the increase of cutting speed. Zhou [31] found that the temperature in ASB increased sharply with the increase of impact speed through impacting pre-notched plates of carbon steel and TC4 alloy. Murr [32] found that the crack speed in ASB increased with the impact speed. ASF in high-speed cutting is a speed-sensitive fracture behavior comparing with the impact tests. In the recent studies, Gu [19] found that the hardened carbon steel was of better work hardening effect and the stress state could be well maintained after ASB formation. The better thermal conductivity of the hardened steel was less influenced by temperature, which resulted in low critical cutting speed. Thus, ASB is difficult to fracture in TA2 alloy comparing with the hardened carbon steel under small cutting thickness. Gu [11] found that the stainless steel exhibited more pressure sensitivity under low rake angle in the cutting tests. The negative rake angle increased the pressure stress and the deformation in PDZ remarkably. Thus, ASF easily occurred under negative rake angle comparing with other cutting tests of titanium alloys [6, 21, 33]. Additionally, austenitic structure in TA2 alloy with poor heat conductivity and pressure stress sensitivity and the stainless steel with good mechanical properties could also result in a lower critical cutting speed under negative rake angle.

It was found that the energy limit value of the TA2 alloy was 3.75×10^9 J/m^2 which was less than the hardened carbon steel and the stainless steel with better mechanical and thermophysical performances. The increase of cutting speed enlarged the strain rate in ASB, shortened the segment deformation time, and suppressed the heat diffusion in band, which aggravated the energy concentration in ASB. Gu [11] found that the time of ASF was very short, but the energy in PDZ continuously concentrated to phrase transformation. The band boundary was distinguished from the surrounding matrix, and the crack propagated along the transformed band. With the serrated segment pushed upward by the cutting tool, the energy in band reached saturation limit resulting in complete fracture in serrated segments along the shear band. It was indicated that the cutting speed was a necessary condition for energy converging. Rittel [34] suggested that the ASB failure was cold energy related in dynamic shear–compress tests of

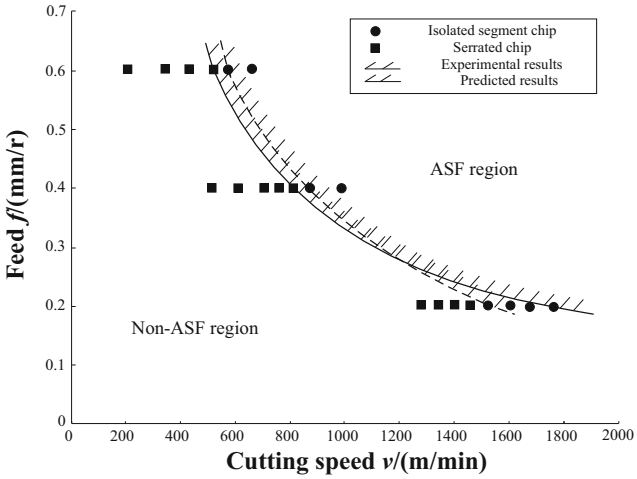

Fig. 8 The experimental and predicted results of ASF in high-speed cutting TA2 alloy

AM50 steel through SHPB tests. He found that the deformation energy in fracture was a relatively constant value of about 4×10^7 J/m^2 in a relative low strain rate. Therefore, this presented model can predict reasonable energy limit within ASB under a wider high speed range.

The theoretical prediction results were compared with the experimental results as shown in Fig. 8. In the figure, the speed regions of ASF and non-ASF were marked. The tendency of the prediction results was coincident with the experimental results. When the cutting speed exceeds the critical cutting speed, the serrated chip would be completely fractured into isolated segment chip. The relative error of the prediction results were controlled in an available range, which could basically meet the actual application requirements in the high-speed machining operations. The prediction bias was caused mainly by the theoretical modeling, including the simplified assumption and assessment methods, in the solution process. The constitutive relation in the tests can also produce some errors between the theoretical and experimental results. The defects and inhomogeneity in material would also influence the experimental results. Therefore, although ASF in high-speed cutting involved some intricacy coupling factors in the fracture process, the critical occurrence conditions can still be assessed effectively through applying this prediction model.

5 Conclusions

The transformation from serrated chip to isolated segment chip was due to the periodic cycle of ASF. The inhomogeneous distribution of stress and heat in PDZ led to various elongations of ductile dimple structure. Based on saturation limit theory, the prediction model of ASF in high-speed cutting TA2 alloy was constructed and the critical cutting

conditions were predicted. The occurrence of ASF in high-speed cutting TA2 alloy was of significant rate-dependent characteristic under negative rake angle. The high cutting speed increased the energy convergence in ASB. Comparing with other titanium alloys, the critical cutting speed of TA2 alloy was relatively low under the negative rake angle and large feed due to the poor heat conductivity and the strong pressure stress sensitivity. The theoretical prediction results of ASF were agreed well with the experimental results, which could basically meet the actual application requirements in the high-speed machining operations.

Acknowledgements Thanks for the assistance of Mold & Die Research Institute of Dalian University of Technology.

Funding This work is supported by National Natural Science Foundation of China (Grant Nos. 51601155 and 51175063).

Appendix

Notation

t Time (s)
v Cutting velocity (m/s)
v_S Shear velocity (m/s)
v_{ch} Chip flow velocity (m/s)
x_i Coordinate axis (m)
$v(x_i)$ Velocity distribution (m/s)
α Damage weakening coefficient
a Rate-related gradient factor
a_c Uncutting thickness (m)
a_{ch} Chip thickness (m)
a_h Thickness of sawtooth (m)
a_β Experimental coefficient
ϕ Shear angle (°)
ϕ' Local shear angle (°)
ψ Angle between free surface plane and shear plane (°)
$P(\xi)$ Momentum (kg m/s)
U Upper side displacement of TP region (m)
X ASB constant
W Boundary shear work of RP region (J/m)
S Shear bandwidth (μm)
h_S Boundary location of PDZ (m)
ξ Boundary location of TP region (m)
$[\overline{\sigma}_i]$ Principal stresses (MPa)
$[\overline{\varepsilon}_i]$ Principal strain
$\left[\dot{\overline{\varepsilon}}_i\right]$ Principal strain rate (s^{-1})
$\hat{\sigma}$ Effective stress (MPa)
$\hat{\varepsilon}$ Effective strain
$\dot{\hat{\varepsilon}}$ Effective strain rate (s^{-1})
σ Pressure stress (MPa)
σ_y Yield strength (MPa)
τ Shear stress (MPa)
$\hat{\tau}$ Equivalent shear stress (MPa)
τ_p Equivalent peak stress (MPa)
$\tau(\gamma, \dot{\gamma}, \theta)$ Constitutive relation (MPa)
γ Shear strain
$\dot{\gamma}$ Shear strain rate (s^{-1})
γ_0 Rake angle (°)
γ_S Strain of RP region
E Elastic model (MPa)
C_E Elastic wave speed (m/s)
C_P Plastic wave speed (m/s)
C_{TP} Thermal-plastic wave speed (m/s)
$\varepsilon_R(t)$ Strain impulse of reflected wave
$\varepsilon_T(t)$ Strain impulse of transmitted wave
A Area of the bar (mm^2)
A_S Area of the sample (mm^2)
l_S Undeformed thickness of RP region
L Length of the sample (mm)
L_P Teeth space (mm)
L_S Shear band space (mm)
θ Temperature (K)
θ_0 Initiate temperature (K)
θ_m Melt point (K).
$\Delta\theta$ Temperature rise (K)
ρ Mass density (kg/m^3)
c Thermal specific capacity (J/kg/K)
χ Thermal diffuse coefficient (m^2/s)
β Taylor and Quinney coefficient
β_0 Incline angle to the free surface (°)
G_{ASB} ASB energy (J/m^2)
G^f_{ASB} Saturation limit (J/m^2)

References

1. Bai Y, Cheng C, Yu S (1986) On evolution of thermo-plastic shear band. Acta Mech Sinica 2:1–7
2. Recht R (1964) Catastrophic thermoplastic shear. J Appl Mech 31: 189–193
3. Komanduri R, Schroeder T, Hazra J, Von Turkovich B, Flom D (1982) On the catastrophic shear instability in high-speed machining of an AISI 4340 steel. J Eng Ind Trans ASME 104:121–131
4. Davies M, Chou Y, Evans C (1996) On chip morphology, tool wear and cutting mechanics in finish hard turning. CIRP Ann Manuf Technol 45:77–82
5. Barry J, Byrne G (2002) The mechanisms of chip formation in machining hardened steels. J Manuf Sci Eng 124:528–535
6. Gente A, Hoffmeister H, Evans C (2001) Chip formation in machining Ti6Al4V at extremely high cutting speeds. CIRP Ann Manuf Technol 50:49–52
7. Shaw M, Vyas A (1998) The mechanism of chip formation with hard turning steel. CIRP Ann Manuf Technol 47:77–82
8. Elbestawi M, Srivastava A, El-Wardany T (1996) A model for chip formation during machining of hardened steel. CIRP Ann Manuf Technol 45:71–76
9. Poulachon G, Moisan A (2000) Hard turning: chip formation mechanisms and metallurgical aspects. J Manuf Sci Eng 122:406

10. Bejjani R, Balazinski M, Attia H, Plamondon P, Lesperance G (2016) Chip formation and microstructure evolution in the adiabatic shear band when machining titanium metal matrix composites. Int J Mach Tools Manuf 109:137–146
11. Gu L, Kang G, Chen H, Wang M (2016) On adiabatic shear fracture in high-speed machining of martensitic precipitation-hardening stainless steel. J Mater Process Technol 234:208–216
12. Minjie W, Chunzheng D, Hongbo L (2004) Experimental study on adiabatic shear behavior in chip formation during orthogonal cutting. Chin J Mech Eng 18:7–10
13. Su G, Liu Z (2010) An experimental study on influences of material brittleness on chip morphology. Int J Adv Manuf Technol 51:87–92
14. Sowerby R, Chandrasekaran N (1989) A proposal for the onset of chip segmentation in machining. Mater Sci Eng A 119:219–229
15. Marusich T, Ortiz M (1995) Modelling and simulation of high-speed machining. Int J Numer Methods Eng 38:3675–3694
16. Xie J, Bayoumi A, Zbib H (1996) A study on shear banding in chip formation of orthogonal machining. Int J Mach Tools Manuf 36: 835–847
17. Guo Y, Yen D (2004) A FEM study on mechanisms of discontinuous chip formation in hard machining. J Mater Process Technol 155:1350–1356
18. Hua J, Shivpuri R (2004) Prediction of chip morphology and segmentation during the machining of titanium alloys. J Mater Process Technol 150:124–133
19. Gu L, Wang M, Duan C (2013) On adiabatic shear localized fracture during serrated chip evolution in high speed machining of hardened AISI 1045 steel. Int J Mech Sci 75:288–298
20. Gu L, Wang M, Chen H, Kang G (2016) Experimental study on the process of adiabatic shear fracture in isolated segment formation in high-speed machining of hardened steel. Int J Adv Manuf Technol 86:671–679
21. Ye GG, Xue SF, Jiang MQ, Tong XH, Dai LH (2013) Modeling periodic adiabatic shear band evolution during high speed machining Ti-6Al-4V alloy. Int J Plast 40:39–55
22. Barry J, Byrne G, Lennon D (2001) Observations on chip formation and acoustic emission in machining Ti6Al4V alloy. Int J Mach Tools Manuf 41:1055–1070
23. Lee W-S, Chiu C-C (2006) Deformation and fracture behavior of 316L sintered stainless steel under various strain rate and relative sintered density conditions. Metall Mater Trans A 37A:3685–3696
24. Marchand A, Duffy J (1988) Experimental study of the formation process of adiabatic Shear bands in a structural steel. J Mech Phys Solids 36:251–283
25. Molinari A (1997) Collective behavior and spacing of adiabatic shear bands. J Mech Phys Solids 45:1551–1575
26. De G, Me K (1987) Growth of unstable thermoplastic Shear with application to steady-wave shock compression in Solids. J Mech Phys Solids 35:95–119
27. Ozel T, Breve R, Zeren E (2006) A methodology to determine work material flow stress and tool-chip interfacial friction properties by using analysis of machining. Trans Am Soc Mech Eng J Manuf Sci Eng 128:119
28. Liao S, Duffy J (1998) Adiabatic shear bands in a Ti-6Al-4V titanium alloy. J Mech Phys Solids 46:2201–2231
29. Yang Y, Li XM, Tong XL, Zhang QM, Xu CY (2011) Effects of microstructure on the adiabatic shearing behaviors of titanium alloy. Mater Sci Eng A 528:3130–3133
30. Dodd B, Bai Y (1989) Width of adiabatic shear bands formed under combined stresses. Mater Sci Technol 5:557–559
31. Zhou M, Rosakis A, Ravichandran G (1996) Dynamically propagating shear bands in impact-loaded prenotched plates—I. Experimental investigations of temperature signatures and propagation speed. J Mech Phys Solids 44:981–1006
32. Murr L, Ramirez A, Gaytan S, Lopez M, Martinez E, Hernandez D, Martinez E (2009) Microstructure evolution associated with adiabatic shear bands and shear band failure in ballistic plug formation in Ti-6Al-4V targets. Mater Sci Eng A 516:205–216
33. Ma W, Li X, Dai L, Ling Z (2012) Instability criterion of materials in combined stress states and its application to orthogonal cutting process. Int J Plast 30-31:18–40
34. Rittel D, Wang Z, Merzer M (2006) Adiabatic shear failure and dynamic stored energy of cold work. Phys Rev Lett 96:75502